

# Sub-100 nm Skyrmions at Zero Magnetic Field in Ir/Fe/Co/Pt Nanostructures

Pin Ho,<sup>1</sup> Anthony K.C. Tan,<sup>1,2</sup> S. Goolaup,<sup>1</sup> A.L. Gonzalez Oyarce,<sup>1</sup> M. Raju,<sup>2</sup> L.S. Huang,<sup>1</sup> Anjan Soumyanarayanan,<sup>1,2,\*</sup> and C. Panagopoulos<sup>2,\*</sup>

<sup>1</sup>*Data Storage Institute, 2 Fusionopolis Way, 138634 Singapore*

<sup>2</sup>*Division of Physics and Applied Physics, School of Physical and Mathematical Sciences, Nanyang Technological University, 637371 Singapore*

Magnetic skyrmions are chiral spin structures that have recently been observed at room temperature (RT) in multilayer thin films. Their topological stability should enable high scalability in confined geometries – a sought-after attribute for device applications. While umpteen theoretical predictions have been made regarding the phenomenology of sub-100 nm skyrmions confined in dots, in practice their formation in the absence of an external magnetic field and evolution with confinement remain to be established. Here we demonstrate the confinement-induced stabilization of sub-100 nm RT skyrmions at zero field (ZF) in Ir/Fe( $x$ )/Co( $y$ )/Pt nanodots over a wide range of magnetic and geometric parameters. The ZF skyrmion size can be as small as  $\sim$ 50 nm, and varies by a factor of 4 with dot size and magnetic parameters. Crucially, skyrmions with varying thermodynamic stability exhibit markedly different confinement phenomenologies. These results establish a comprehensive foundation for skyrmion phenomenology in nanostructures, and provide immediate directions for exploiting their properties in nanoscale devices.

## A. INTRODUCTION

The whirling arrangement of spins that defines a magnetic skyrmion arises from chiral relativistic interactions in magnetic materials lacking inversion symmetry<sup>1,2</sup>. The topologically protected spin structure of skyrmions manifests in their emergent behavior as distinct magnetic quasiparticles<sup>3</sup>, with individual addressability, and current-induced creation and dynamics<sup>4,5</sup>. The discovery of RT skyrmions in multilayer films<sup>6–10</sup>, material platforms of demonstrable technological relevance, has generated an explosion of interest in investigating these topological quasiparticles in device-relevant configurations<sup>11–13</sup>. In particular, device proposals build upon their lateral mobility in wires<sup>5,14,15</sup>, and their manipulation in dots<sup>5,16,17</sup>. Harnessing the potential of nanoscale skyrmions calls for an immediate understanding of their phenomenology in confined geometries.

The interest surrounding skyrmions confined in dots is piqued by the knowledge amassed on conventional nanomagnetic dots, and their technological relevance<sup>18</sup>. The topological stability of skyrmions<sup>19</sup> could enable dot devices with nanometer scalability<sup>4</sup>, with ease of detection<sup>4,20,21</sup>, and energy-efficient manipulation<sup>4,17,22,23</sup>. In particular, they could be used in magnetic tunnel junction (MTJ)-like configurations, with applications in memory<sup>22,23</sup>, logic<sup>11</sup>, oscillators<sup>24,25</sup>, and microwave detectors<sup>16</sup>. This has prompted a flurry of theoretical and experimental efforts to establish the phenomenology of confined skyrmions. Notably, theoretical works predict the scaling of skyrmion size and stability with geometric and magnetic parameters<sup>5,26–31</sup>. Experimental studies on multilayers have reported  $> 150$  nm skyrmion bubbles in the absence of external fields, with the chiral spin structure stabilized by the additional presence of dipolar interactions at larger length scales<sup>7,8,32</sup>. However, skyrmions with sub-100 nm sizes, thus far stabilized

at finite external magnetic fields<sup>6,10</sup>, have yet to exhibit confinement effects. Till date, the zero field (ZF) stabilization of sub-100 nm skyrmions in dots, the role of confinement in governing skyrmion properties, and its interplay with magnetic parameters – remain to be established.

Here we report the ZF stabilization of sub-100 nm RT skyrmions in nanodots of Ir/Fe( $x$ )/Co( $y$ )/Pt multilayer films. We utilize magnetic force microscopy (MFM) and micromagnetic simulations to establish their stability over a wide range of magnetic and geometric parameters. In our patterned dots, the ZF skyrmion size, as small as  $\sim$  50 nm, varies by a factor of 4 with confinement and magnetic interactions. In particular, confined skyrmions exhibit markedly different phenomenologies with varying thermodynamic stability. Our results provide immediate directions for tailoring skyrmions properties to confined geometries geared to device applications.

## B. CONFINED STATES IN MULTILAYERS

The ground state configuration of a magnetic multilayer nanostructure is determined by the confluence of magnetic interactions. The exchange interaction, characterized by the stiffness ( $A$ ), aligns neighboring spins parallel, and favors a uniformly magnetized (UM) state (Fig. 1b, left), with orientation determined by the effective out-of-plane (OP) anisotropy,  $K_{\text{eff}}$ . In contrast, the interfacial Dzyaloshinskii-Moriya interaction (DMI,  $D$ ) prefers a winding spin arrangement, leading to a labyrinthine stripe (LS) state (Fig. 1b, right)<sup>33</sup>. The competition between  $D$ ,  $A$ , and  $K_{\text{eff}}$  can form Néel-textured skyrmions (SK, Fig. 1b, centre)<sup>4</sup>, thermodynamically stable entities for  $\kappa = \pi D / 4\sqrt{AK_{\text{eff}}} > 1$ <sup>1,3</sup>. Notably, confined geometries can dramatically influence the ground state configuration<sup>8,26,34–37</sup>, potentially favoring the ZF stabilization of skyrmions<sup>5,26</sup>. The added presence of interlayer dipolar coupling in multilayer stacks<sup>31,37?</sup>,

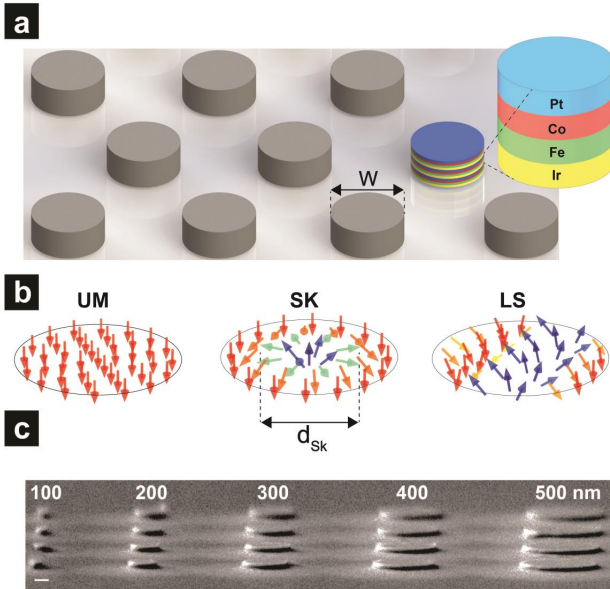


**FIG. 1. Confined Magnetic States in Multilayer Nanodots.** (a) Schematic array of sub- $\mu\text{m}$  dots (diameter  $W$ ) composed of Ir/Fe( $x$ )/Co( $y$ )/Pt multilayers. Inset shows the sequence of Ir, Fe, Co, and Pt layers forming a stack. (b) Schematic spin textures corresponding to the three distinct states expected in such nanodots: uniform magnetization (UM: left), Néel skyrmion with size  $d_{\text{Sk}}$  (SK: centre), and labyrinthine stripes (LS: right). (c) Cross-sectional scanning electron microscope (SEM) image (scale bar: 100 nm) of a  $[\text{Ir}/\text{Fe}/\text{Co}/\text{Pt}]_{20}$  dot array with  $W$  from 100 – 500 nm.

and long-range intralayer dipolar interactions<sup>8</sup>, can also influence the ground state – the latter being key to the pioneering works reporting the stability of confined skyrmion ‘bubbles’<sup>7–9,31,32</sup>. Motivated by this, we focus on the ZF stabilization of sub-100 nm Néel skyrmions in confined geometries<sup>13</sup>.

The stability and size of confined skyrmions is expected to be markedly influenced by magnetic interactions (e.g.  $D$ ,  $A$ , and  $K_{\text{eff}}$ ) and geometric parameters (here,  $W$ )<sup>26,31,37</sup>. The multilayer Ir/Fe( $x$ )/Co( $y$ )/Pt, wherein magnetic interactions can be tailored by the Fe( $x$ )/Co( $y$ ) composition, is an aptly suited platform for establishing confined skyrmion phenomenology.  $[\text{Ir}(10)/\text{Fe}(x)/\text{Co}(y)/\text{Pt}(10)]_{20}$  stacks (layer thicknesses in Å in parentheses) host Néel-textured skyrmions<sup>38</sup> with tunable size ( $2\times$ ), thermodynamic stability ( $10\times$ ), and density ( $10\times$ ) across compositions<sup>10</sup> (details in § F). Here we investigate confined skyrmions in dots ( $W$ : 100 – 3000 nm) patterned from these stacks (e.g. Fig. 1c, details in § F). The five samples studied here, described henceforth by their Fe( $x$ )/Co( $y$ ) composition, allow us to vary  $D/A$  from 15 – 18  $\text{nm}^{-1}$  and  $K_{\text{eff}}$  from 0.01 – 0.25  $\text{MJ/m}^3$ , corresponding to an order of magnitude modulation of  $\kappa$  (0.8–6.3, Fig. 4a, details in SSI 1). The magnetic configuration was imaged by MFM using ultra-low moment tips for high-resolution, non-perturbative imaging, after negative OP saturation (see § F). The excellent agreement observed between the magnetic texture evolution for our  $W \geq 1000$  nm

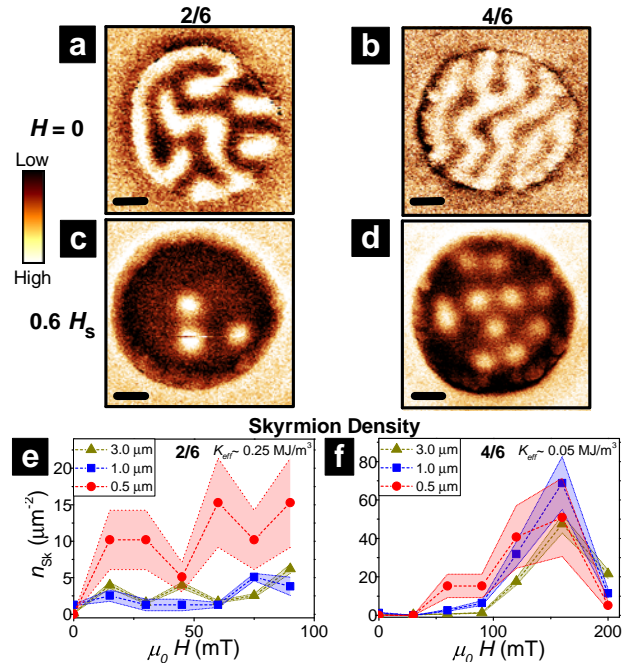


**FIG. 2. Confinement Effects in Sub- $\mu\text{m}$  Dots.** (a-d) MFM images (scale bar: 100 nm) of  $W = 500$  nm dots after negative saturation for Fe(2)/Co(6) (a, c) and Fe(4)/Co(6) (b, d) stacks, respectively. At  $H = 0$ , (a-b) show LS states; At  $H \approx 0.6 H_S$  (c-d) show SK states, in isolated (c) and lattice (d) configurations, respectively. (e-f) Measured skyrmion density,  $n_{\text{Sk}}$ , as a function of  $H$ , for dots with varying  $W$  for samples Fe(2)/Co(6) (e) and Fe(4)/Co(6) (f) respectively. Shaded regions represent error bars.

dots with corresponding film-level results (SSI 3) establishes a firm foundation for investigating confinement effects in sub- $\mu\text{m}$  geometries.

We begin by examining the emergence of confinement effects as  $W$  is reduced to 500 nm. Consistent with film-level results<sup>10</sup>, we observe an LS state at ZF (Fig. 2a,b) transforming into sub-100 nm skyrmions at finite OP fields ( $H$ , Fig. 2c,d). However, the skyrmion density,  $n_{\text{Sk}}$ , displays a striking contrast with  $W$ -evolution across samples. For Fe(2)/Co(6) ( $K_{\text{eff}} = 0.25 \text{ mJ/m}^3$ , Fig. 2e),  $n_{\text{Sk}}$  is consistently higher in 500 nm dots, by a factor of 3, as compared to larger dots and films. This increase in  $n_{\text{Sk}}$  with smaller  $W$  can be attributed to the enhancement of the in-plane (IP) demagnetization field with confinement<sup>7,8</sup>. Meanwhile, for Fe(4)/Co(6) ( $K_{\text{eff}} = 0.06 \text{ mJ/m}^3$ , Fig. 2f),  $n_{\text{Sk}}(H)$  is consistent across  $W$  down to 500 nm, and  $\sim 5 – 10\times$  higher than for Fe(2)/Co(6). Indeed  $n_{\text{Sk}}$  is known to increase with reducing  $K_{\text{eff}}$  as the energy barrier for domain nucleation is lowered<sup>10</sup>. Importantly, the constancy of  $n_{\text{Sk}}$  with  $W$  for Fe(4)/Co(6) – which already hosts a dense skyrmion lattice – offers an orthogonal tuning parameter. This suggests that utilizing the synergy between magnetic tuning and confinement in sub-500 nm dots is a promising route for ZF skyrmion stabilization.

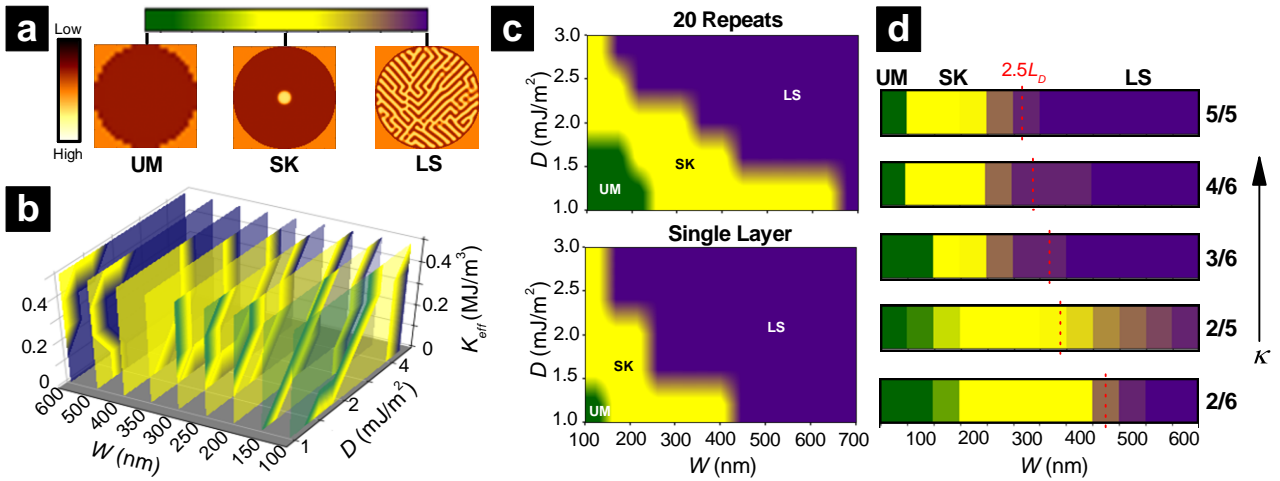


**FIG. 3. Simulated Evolution of ZF Magnetic States.** Micromagnetic simulations of the ZF phase diagram for  $[Ir/Fe(x)/Co(y)/Pt]_{20}$  dots. (a) Magnetic textures obtained (examples shown) are identified as UM (left: green), SK (centre: yellow), or LS (right: blue) respectively. Phase diagrams with Fe(2)/Co(6) parameters, for: (b) 20 repeats (top) and single layer (bottom):  $D$ ,  $K_{\text{eff}}$ , and  $W$  are varied over a range of likely values. SK is the expected ground state over a broad, intermediate set of parameters. (d) Expected evolution of magnetic states in dots with  $W$  ranging from 50 – 600 nm across the five samples (shown with increasing  $\kappa$ , parameters in Fig. 4a, SSI 1).

### C. CONFINED ZERO FIELD SKYRMIONS

We performed a comprehensive set of multilayer micromagnetic simulations to map the evolution of magnetic states for Ir/Fe( $x$ )/Co( $y$ )/Pt dots (details in § F, parameters in SSI 1). The relaxed magnetic state at ZF, following the introduction of a skyrmion, was examined over a range of parameters to determine the magnetic phase diagram<sup>5,7</sup>. Fig. 3b shows such a ZF phase diagram (magnetic states in Fig. 3a) with varying  $W$  (100–600 nm),  $D$  (1 – 4 mJ/m<sup>2</sup>),  $K_{\text{eff}}$  (0 – 0.5 MJ/m<sup>3</sup>), and nominal parameters of Fe(2)/Co(6) (SSI 4). While the LS phase is observed at large  $W$ , the reduction in magnetostatic energy for  $W \lesssim 500$  nm shrinks the stable domain wall size, and instead favors the formation of an SK phase<sup>26</sup>. As  $W$  is reduced further (e.g. below  $\sim 100$  nm), the exchange energy eventually dominates, leading to the UM phase. Moreover, the interplay between confinement and magnetic parameters determines the window for SK stability in dots, which is explored here.

First, a comparison of the phase diagram for the Fe(2)/Co(6) multilayer (Fig. 3c, top) with the corresponding single layer (Fig. 3c, bottom) shows the SK phase persisting over a much larger  $W$  range in the multilayer. The addition of interlayer dipolar coupling, introduced by multilayer stacking, is key to this increased SK stability<sup>31?</sup>. Next, an inspection of the confined magnetic states across samples (Fig. 3d, optimal parameters) suggests that ZF skyrmions should be observable for all compositions. Finally, the SK phase may be observed for  $W \lesssim 2.5 L_D$  ( $L_D$  is the film-level domain periodicity), and its stability in smaller dots could be enhanced with increasing  $\kappa$ . These results provide promise and specific directions for stabilizing skyrmions in Ir/Fe( $x$ )/Co( $y$ )/Pt nanostructures.

We now turn to MFM images of ZF magnetic textures for  $W < 500$  nm dots, shown for three samples in Fig. 4b (remainder in SSI 3). Consistent with simulations (Fig. 3d), reducing  $W$  (500 – 150 nm: Fig. 4b, right to left), results in a gradual transition from LS to SK phases, and eventually to the UM phase. Crucially, sub-100 nm skyrmions are stabilized at ZF, *prima facie* by confinement effects, across all Ir/Fe( $x$ )/Co( $y$ )/Pt compositions. In some cases, however, nominally identical dots are found to exhibit different ZF states, likely due to the granularity of sputtered multilayer films<sup>32,39,40</sup>, or fabrication process variations (§ F, SSI 2). This variability is mitigated by determining the statistically averaged behavior of 12 dots for each  $W$  across samples. The evolution of ZF skyrmion state probability thus obtained,  $P_{\text{SK}}$ , is further examined.

Histogram plots of  $P_{\text{SK}}(W)$  across samples (Fig. 4c) evidence a stable SK phase over a wide range of magnetic (Fig. 4a) and geometric parameters. In line with simulations (Fig. 3d), the increased skyrmion stability in multilayers underscores the vital role of interlayer dipolar interactions. Next, while the peak  $P_{\text{SK}}$  appears to shift to lower  $W$  with  $\kappa$  for  $\kappa \lesssim 1$ , this trend, expected from simulations, does not persist for  $\kappa > 1$ . For  $W < 200$  nm (Fig. 4c shaded region), low yield in our patterning process precludes a statistically meaningful comparison across  $\kappa$  (§ F). More surprising is the persistence of the SK phase for  $\kappa > 1$  at larger  $W$ , and particularly, the observation of multi-skyrmion (m-SK) configurations (e.g. Fig. 4b-i, 300 nm; Fig. 4c, red). While thermodynamically stable skyrmions ( $\kappa > 1$ ) form ordered lattices at finite fields<sup>1,2,4,10,35</sup>, the emergence of m-SK configurations at ZF emphasizes a strong interplay of magnetic and confinement effects that was not considered in previous simulations. Indeed, when simulations are re-

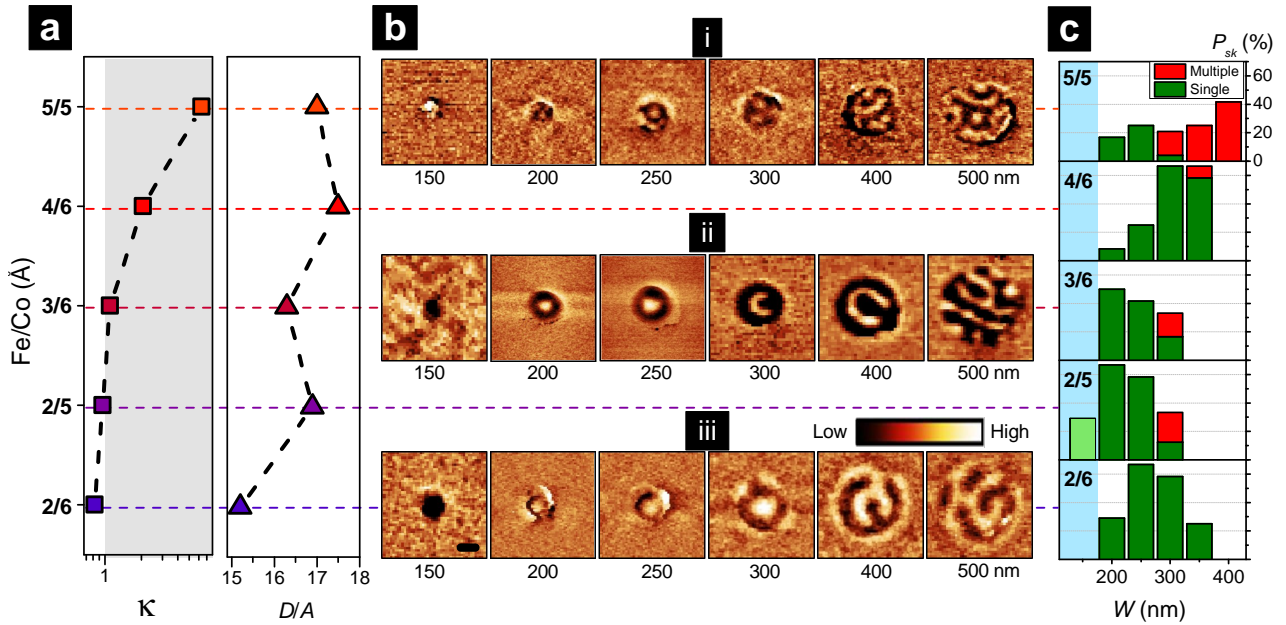


**FIG. 4. Imaging Confined ZF Skyrmions.** (a) Variation of the parameters:  $\kappa$  and  $D/A$  across the studied samples. (b) MFM images at ZF (scale bar: 100 nm) showing the magnetic states in dots with  $W$  ranging from 150 – 500 nm, for samples Fe(2)/Co(6), Fe(3)/Co(6), and Fe(5)/Co(5) respectively. The images, in several cases, show ZF skyrmions at intermediate  $W$ , while UM and LS phases are observed for smaller and larger dots respectively. (c) Empirical ZF skyrmion nucleation probability,  $P_{Sk}$  (averaged over 12 nominally identical dots), as a function of  $W$  for all five samples. Shaded blue region ( $W < 200$  nm) indicates a low yield from the patterning process. Both single (green bars) and multiple (red bars) skyrmion configurations are observed.

peated with the initialized skyrmion number,  $N_i > 1$  (Fig. 5d, SSI 4)<sup>7,34</sup> – m-SK states are found to be stable for  $\kappa > 1$  dots (Fig. 5d-i). In contrast, m-SK states are consistently absent in  $\kappa < 1$  dots – both in experiments (Fig. 4b-iii) and simulations (Fig. 5d-iii) – only single skyrmions are formed across  $W$ . These results demonstrate magnetic and geometric tuning of confined ZF skyrmion stability.

#### D. VARIATION OF SKYRMION SIZE

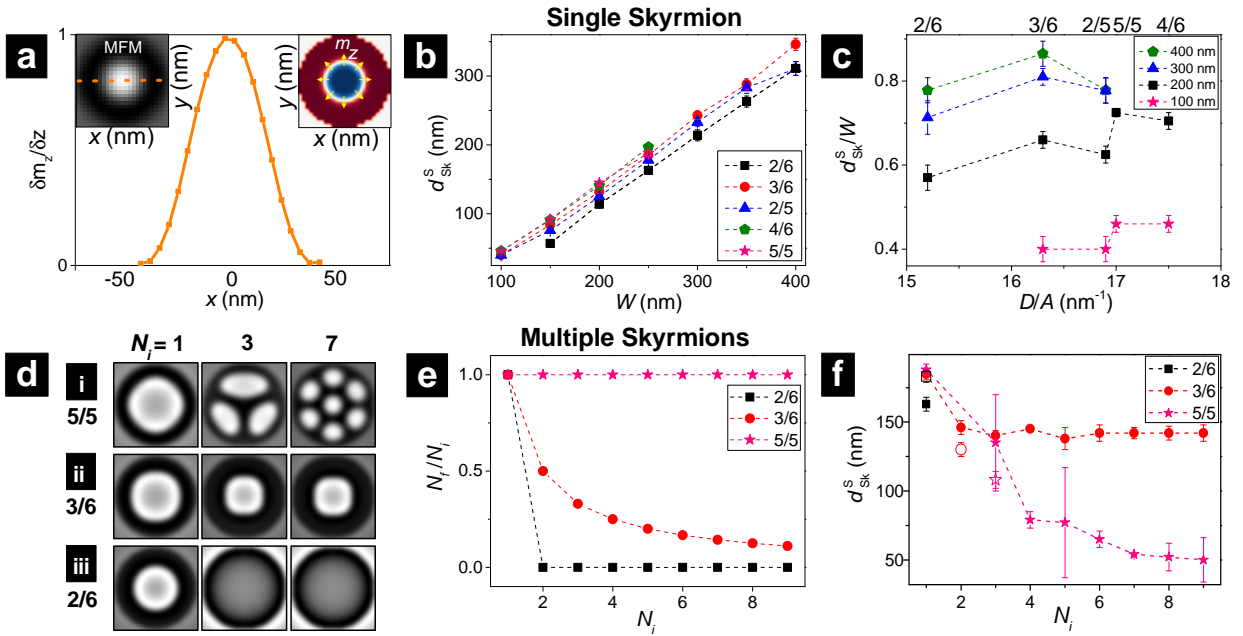
A visible modulation in the measured skyrmion size,  $d_{Sk}^M$ , across magnetic (vertical) and geometric (horizontal) parameters, is clearly seen in Fig. 4b. We begin by examining the trends in simulated skyrmion size,  $d_{Sk}^S$  (e.g. Fig. 5a, details in § F), to interpret the experimental trends. Fig. 5b summarizes the simulated  $d_{Sk}^S$  trends for  $N_i = 1$ , showing a near-identical  $W$ -dependence across samples. This corresponds to a weak dependence of the normalized size  $d_{Sk}^S/W$  on magnetic parameters, e.g.  $D/A$  (Fig. 5c), consistent with recent multilayer simulations by other groups<sup>31,37</sup>. However, such insensitivity of  $d_{Sk}^S$  to magnetic parameters is in stark contrast with a visual inspection of MFM data (Fig. 4a-b). A reconciliation should be established between simulated and measured  $d_{Sk}$  trends by accounting for the aforementioned m-SK stability for  $\kappa \gtrsim 1$ .

The relaxed magnetic configuration for  $N_i > 1$  simulations (Fig. 5d-e for  $W = 250$  nm) shows a marked transformation with varying  $\kappa$ , in line with experimental trends (Fig. 4b). First, for  $\kappa < 1$  (Fig. 5d-iii), only single skyrmions can be stabilized,

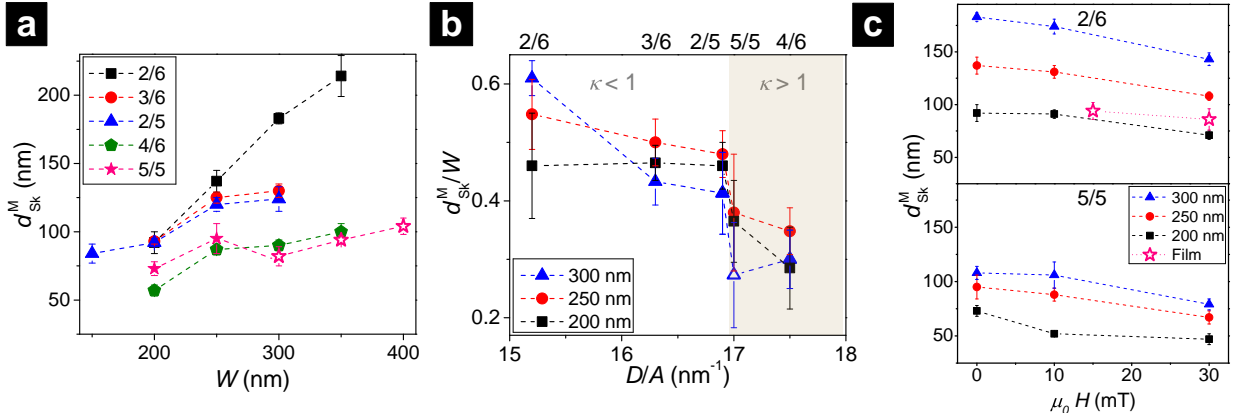
and only with  $N_i = 1$ ;  $N_i > 1$  simulations relax to a UM state. Next, for  $\kappa \sim 1$  (Fig. 5d-ii),  $N_i > 1$  simulations relax to a single skyrmion, albeit with reduced  $d_{Sk}^S$ . Finally, for  $\kappa > 1$  (Fig. 5d-i), m-SK configurations are formed for  $N_i > 1$ , while  $d_{Sk}^S$  reduces and plateaus for larger  $N_i$ . Importantly, these  $d_{Sk}^S$  values (Fig. 5f: filled) agree well with measured  $d_{Sk}^M$  trends (Fig. 5f: empty) when  $N_i$  is appropriately considered. The inclusion of magnetic granularity<sup>39,40</sup> and inter-layer coupling<sup>32</sup> in future could further improve the quantitative agreement of  $d_{Sk}^S$  with experiments.

Fig. 6a summarizes the measured ZF  $d_{Sk}^M$  trends, showing an overall factor of 4 reduction – from  $\sim 200$  nm down to  $\sim 50$  nm. Here, the  $d_{Sk}^M$  lowest values represent an overestimate from the implicit convolution with a  $\sim 30$  nm MFM probe (§ F).  $d_{Sk}^M$  is monotonically reduced with increased confinement for all samples, with up to  $2.5\times$  reduction for Fe(2)/Co(6). Similarly, for a given dot size,  $d_{Sk}^M$  varies by up to  $2.5\times$  across samples. Most interesting in Fig. 6a is the marked disparity in the  $W$ -dependence of  $d_{Sk}^M$ . The confinement gradient, defined as  $\delta d_{Sk}^M / \delta W$ , reduces by  $4\times$  across samples. This observation, while incongruous with  $N_i = 1$  simulations for  $\kappa > 1$  (Fig. 5b), is consistent with the behavior of m-SK states (Fig. 5f).

Finally we examine the evolution of  $d_{Sk}^M$  with  $D/A$  (Fig. 6b) and  $H$  (Fig. 6c), in the context of extensive predictions of these trends<sup>5,6,26,28,30,31,37</sup>. Fig. 6b shows that the normalized size,  $d_{Sk}^M/W$ , reduces monotonically with increasing  $D/A$  – with a sharp jump at  $\kappa \sim 1$ . The sudden factor-of-2 reduction



**FIG. 5. Simulated Variation of Skyrmion Size.** (a) Simulated MFM profile of a Néel skyrmion in a 100 nm Fe(3)/Co(6) dot, extracted from a linecut (dashed orange) across the simulated MFM image (left inset, grayscale). A Gaussian fit to the profile gives  $d_{Sk}^S$ . Right inset shows the corresponding magnetization ( $m_z$ , color scale), with yellow arrows indicating IP Néel texture. (b)  $d_{Sk}^S$  trend for a single skyrmion initialized and relaxed in a dot, with varying  $W$  across samples. (c) Modulation of  $d_{Sk}^S / W$  (values from b) with  $D/A$  across samples. (d-f) Simulated initialization of varying numbers of skyrmions (number:  $N_i$ ) in a  $W = 250$  nm dot across three samples: Fe(2)/Co(6), Fe(3)/Co(6) and Fe(5)/Co(5). (d) Grayscale MFM images of the relaxed state for three values of  $N_i$ , showing varying numbers of stabilized skyrmions ( $N_f$ ). (e) Observed trend in  $N_f$  for  $N_i$  ranging from 1 to 9. (f) The variation in  $d_{Sk}^S$  with  $N_i$  (solid symbols), with  $N_i > 1$  simulations giving qualitatively different trends across samples. Open symbols show measured  $d_{Sk}^M$  values from experiments for comparison.



**FIG. 6. Measured Variation of Skyrmion Size.** (a) Summary of measured  $d_{Sk}^M$  values at ZF (isotropic Gaussian fits to MFM data) for all samples across dot sizes. Visible trends in  $d_{Sk}^M$  and extent of  $W$ -dependence are observed across samples. Open symbols are derived from m-SK configurations. (b) The ratio  $d_{Sk}^M / W$  for several values of  $W$ , plotted against  $D/A$  (c.f. Fig. 5c). (c) Field dependence of  $d_{Sk}^M$  for two representative samples – Fe(2)/Co(6) (film-level results included for comparison) and Fe(5)/Co(5) – for several values of  $W$ .

in  $d_{Sk}^M / W$  consistently across all  $W$ , is indicative of a fundamental change in the behavior of confined skyrmions around  $\kappa \simeq 1$ , especially in light of recent predictions<sup>31</sup>. Next, Fig. 6c shows the expected reduction in  $d_{Sk}^M$  with increasing  $H$  across samples. However, the 20–30% reduction (for 0–30 mT) seen here is considerably less than the 2–3× reduction reported for larger confined skyrmions with similar fields<sup>7,8,32</sup>. Furthermore, the ZF trend of  $d_{Sk}^M(W)$  is found to persist at finite fields – smaller dots consistently host smaller skyrmions – in contrast with

prior reports<sup>6</sup>. This highlights the demonstrable robustness of confinement effects in Ir/Fe/Co/Pt dots. Meanwhile, the marked modulation with magnetic parameters suggests that a mechanistic understanding of  $d_{Sk}^M$ , and its relationship within intrinsic and extrinsic interactions, merits a detailed theoretical investigation.

## E. OUTLOOK

We have presented a comprehensive picture of formation and evolution of skyrmions at ZF by tailoring

confinement effects in Ir/Fe( $x$ )/Co( $y$ )/Pt dots. Sub-100 nm skyrmions are stabilized at ZF over a wide range of magnetic and geometric parameters by intrinsic ( $\kappa$ ), interlayer, and confinement-induced magnetic interactions. The size of these ZF skyrmions, here as small as  $\sim 50$  nm, varies with magnetic and geometric parameters, by up to  $\sim 2.5 \times$  in either case. Finally, the ZF stability of multiple skyrmion configurations for  $\kappa \gtrsim 1$  – and the stark contrast in their size evolution across  $\kappa = 1$  – suggest a strong synergy of thermodynamic and confinement effects. These results provide a firm foundation for tailoring the phenomenology of nanoscale skyrmion in confined geometries.

First, the sub-100 nm Néel skyrmions at ZF reported here show markedly different physical characteristics from confined skyrmion bubbles<sup>7,8,32</sup>. This indicates that despite their nominally identical topological characteristics<sup>12,13</sup>, exploring the stability<sup>31</sup>, detection<sup>21</sup>, and dynamics<sup>39</sup> of these spin structures could require independent lines of investigation. Our comprehensive investigation of confined Néel skyrmions offers a firm foundation tailor-made for such efforts. Second the manifestly distinct trends in skyrmion configuration and size with varying  $\kappa$  go beyond existing predictions<sup>5,26,28,30,31</sup>. While recent studies have incorporated the effects of granularity<sup>32,40</sup>, interlayer coupling<sup>6</sup>, and dipolar interactions<sup>31,37</sup>, we posit that future studies of confined skyrmions would benefit from harnessing their varying behavior with thermodynamic stability. Finally, the elastic tuning of skyrmion size with confinement opens up the exciting possibility of designer magnetic lattices with topological properties – with the potential to engineer frustration, criticality, and topology under ambient conditions<sup>41</sup>.

Crucially, the first realization of sub-100 nm ZF skyrmions in a device-relevant geometry prompts their immediate employment along technological lines, especially within perpendicular MTJ devices. First, the demonstrable modulation of their stability and size with magnetic interactions and confinement enables mechanistic investigations of skyrmion creation<sup>4</sup>, detection<sup>20,21</sup>, and dynamics<sup>5</sup> in ambient, device-ready conditions. Next, their sub-100 nm size and ZF stability over a wide range would enable energy-efficient microwave detectors<sup>16</sup>, oscillators<sup>25</sup>, spin valves<sup>24</sup>, and magnonic crystals<sup>42</sup>. Finally, we note that their topological stability and malleability with confinement are particularly suited for highly scalable realizations of random access memory<sup>43</sup> and synaptic computing<sup>44</sup>.

*Letters* **87**, 037203 (2001).

- [2] N. Nagaosa and Y. Tokura, *Nature Nanotechnology* **8**, 899 (2013).
- [3] A. Soumyanarayanan, N. Reyren, A. Fert, and C. Panagopoulos, *Nature* **539**, 509 (2016).
- [4] N. Romming, C. Hanneken, M. Menzel, J. E. Bickel, B. Wolter, K. von Bergmann, A. Kubetzka, and R. Wiesendanger, *Science* **341**, 636 (2013).
- [5] J. Sampaio, V. Cros, S. Rohart, A. Thiaville, and A. Fert, *Nature Nanotechnology* **8**, 839 (2013).
- [6] C. Moreau-Luchaire, C. Moutafis, N. Reyren, J. Sampaio, C. A. F. Vaz, N. Van Horne, K. Bouzehouane, K. Garcia, C. Deranlot, P. Warnicke, P. Wohlhüter, J.-M. George, M. Weigand, J. Raabe, V. Cros, and A. Fert, *Nature Nanotechnology* **11**, 444 (2016).
- [7] S. Woo, K. Litzius, B. Krüger, M.-y. Im, L. Caretta, K. Richter, M. Mann, A. Krone, R. M. Reeve, M. Weigand, P. Agrawal, I. Lemesh, M.-A. Mawass, P. Fischer, M. Kläui, and G. S. D. Beach, *Nature Materials* **15**, 501 (2016).
- [8] O. Boulle, J. Vogel, H. Yang, S. Pizzini, D. de Souza Chaves, A. Locatelli, T. O. Mentes, A. Sala, L. D. Buda-Prejbeanu, O. Klein, M. Belmeguenai, Y. Rousigné, A. Stashkevich, S. M. Chérif, L. Aballe, M. Forster, M. Chshiev, S. Auffret, I. M. Miron, and G. Gaudin, *Nature Nanotechnology* **11**, 449 (2016).
- [9] W. Jiang, P. Upadhyaya, W. Zhang, G. Yu, M. B. Jungfleisch, F. Y. Fradin, J. E. Pearson, Y. Tserkovnyak, K. L. Wang, O. Heinonen, S. G. E. te Velthuis, and A. Hoffmann, *Science* **349**, 283 (2015).
- [10] A. Soumyanarayanan, M. Raju, A. L. G. Oyarce, A. K. C. Tan, M.-Y. Im, A. P. Petrovic, P. Ho, K. H. Khoo, M. Tran, C. K. Gan, F. Ernult, and C. Panagopoulos, *Nature Materials* **16**, 898 (2017).
- [11] W. Kang, Y. Huang, X. Zhang, Y. Zhou, and W. Zhao, *Proceedings of the IEEE* **104**, 2040 (2016).
- [12] G. Finocchio, F. Büttner, R. Tomasello, M. Carpentieri, and M. Kläui, *Journal of Physics D: Applied Physics* **49**, 423001 (2016).
- [13] A. Fert, N. Reyren, and V. Cros, *Nature Reviews Materials* **2**, 17031 (2017).
- [14] J. Iwasaki, M. Mochizuki, and N. Nagaosa, *Nature Nanotechnology* **8**, 742 (2013).
- [15] X. Zhang, Y. Zhou, and M. Ezawa, *Nature Communications* **7**, 10293 (2016).
- [16] G. Finocchio, M. Ricci, R. Tomasello, A. Giordano, M. Lanuzza, V. Puliafito, P. Burrascano, B. Azzerboni, and M. Carpentieri, *Applied Physics Letters* **107**, 262401 (2015).
- [17] B. Zhang, W. Wang, M. Beg, H. Fangohr, and W. Kuch, *Applied Physics Letters* **106**, 102401 (2015).
- [18] S. A. Wolf, J. Lu, M. R. Stan, E. Chen, and D. M. Treger, *Proceedings of the IEEE* **98**, 2155 (2010).
- [19] J. Hagemeister, N. Romming, K. von Bergmann, E. Y. Vedmedenko, and R. Wiesendanger, *Nature Communications* **6**, 8455 (2015).
- [20] C. Hanneken, F. Otte, A. Kubetzka, B. Dupé, N. Romming, K. von Bergmann, R. Wiesendanger, and S. Heinze, *Nature Nanotechnology* **10**, 1039 (2015).
- [21] R. Tomasello, M. Ricci, P. Burrascano, V. Puliafito, M. Carpentieri, and G. Finocchio, *AIP Advances* **7**, 056022 (2017).
- [22] Y. Nakatani, M. Hayashi, S. Kanai, S. Fukami, and H. Ohno, *Applied Physics Letters* **108**, 152403 (2016).
- [23] D. Bhattacharya and J. Atulasimha, ArXiv e-prints

\* Correspondence should be addressed to **A.S.** (souma@dsi.a-star.edu.sg) or **C.P.** (christos@ntu.edu.sg)

[1] A. N. Bogdanov and U. K. Rößler, *Physical Review*

- (2017), arXiv:1707.07777 [cond-mat.mes-hall].
- [24] Y. Zhou, E. Iacocca, A. A. Awad, R. K. Dumas, F. C. Zhang, H. B. Braun, and J. Åkerman, *Nature Communications* **6**, 8193 (2015).
- [25] F. Garcia-Sanchez, J. Sampaio, N. Reyren, V. Cros, and J.-V. Kim, *New Journal of Physics* **18**, 075011 (2016).
- [26] S. Rohart and A. Thiaville, *Physical Review B* **88**, 184422 (2013).
- [27] K. Y. Guslienko, *IEEE Magnetics Letters* **6**, 4000104 (2015).
- [28] J. Mulkers, B. van Waeyenberge, and M. V. Milošević, *Physical Review B* **95**, 144401 (2017).
- [29] A. Kolesnikov, A. Samardak, M. Stebliy, A. Ognev, L. Chebotkevich, A. Sadovnikov, S. Nikitov, Y. J. Kim, I. H. Cha, and Y. K. Kim, *Journal of Magnetism and Magnetic Materials* **429**, 221 (2017).
- [30] R. Tomasello, K. Y. Guslienko, M. Ricci, A. Giordano, J. Barker, M. Carpentieri, O. Chubykalo-Fesenko, and G. Finocchio, ArXiv e-prints (2017), ArXiv e-prints:1706.07569 [cond-mat.mes-hall].
- [31] M. Zelent, J. Tóbik, M. Krawczyk, K. Y. Guslienko, and M. Mruczkiewicz, ArXiv e-prints (2017), arXiv:1708.01149 [cond-mat.mes-hall].
- [32] K. Zeissler, M. Mruczkiewicz, S. Finizio, J. Raabe, P. M. Shepley, A. V. Sadovnikov, S. A. Nikitov, K. Fallon, S. McFadzean, S. McVitie, T. A. Moore, G. Burnell, and C. H. Marrows, ArXiv e-prints (2017), arXiv:1706.01065 [cond-mat.mes-hall].
- [33] M. Heide, G. Bihlmayer, and S. Blügel, *Physical Review B* **78**, 140403 (2008).
- [34] M. Beg, R. Carey, W. Wang, D. Cortés-Ortuño, M. Vousden, M.-A. Bisotti, M. Albert, D. Chernyshenko, O. Hovorka, R. L. Stamps, and H. Fangohr, *Scientific Reports* **5**, 17137 (2015).
- [35] X. Zhao, C. Jin, C. Wang, H. Du, J. Zang, M. Tian, R. Che, and Y. Zhang, *Proceedings of the National Academy of Sciences* **113**, 4918 (2016).
- [36] C. Jin, Z.-A. Li, A. Kovács, J. Caron, F. Zheng, F. N. Rybakov, N. S. Kiselev, H. Du, S. Blügel, M. Tian, Y. Zhang, M. Farle, and R. E. Dunin-Borkowski, *Nature Communications* **8**, 15569 (2017).
- [37] N. Vidal-Silva, A. Riveros, and J. Escrig, *Journal of Magnetism and Magnetic Materials* **443**, 116 (2017).
- [38] A. Yagil, A. Almoalem, A. Soumyanarayanan, A. K. C. Tan, M. Raju, C. Panagopoulos, and O. M. Auslaender, ArXiv e-prints (2017), arXiv:1705.07608 [physics.app-ph].
- [39] W. Legrand, D. Maccariello, N. Reyren, K. Garcia, C. Moutafis, C. Moreau-Luchaire, S. Collin, K. Bouzehouane, V. Cros, and A. Fert, *Nano Letters* **17**, 2703 (2017).
- [40] R. Juge, S.-G. Je, D. d. S. Chaves, S. Pizzini, L. D. Buda-Prejbeanu, L. Aballe, M. Foerster, A. Locatelli, T. O. Mentes, A. Sala, F. Maccherozzi, S. S. Dhesi, S. Auffret, G. Gaudin, J. Vogel, and O. Boulle, ArXiv e-prints (2017), arXiv:1706.01726 [cond-mat.mes-hall].
- [41] C. Nisoli, R. Moessner, and P. Schiffer, *Reviews of Modern Physics* **85**, 1473 (2013).
- [42] A. V. Chumak, V. I. Vasyuchka, A. A. Serga, and B. Hillebrands, *Nature Physics* **11**, 453 (2015).
- [43] D. Apalkov, B. Dieny, and J. M. Slaughter, *Proceedings of the IEEE* **104**, 1796 (2016).
- [44] J. Torrejon, M. Riou, F. A. Araujo, S. Tsunegi, G. Khalsa, D. Querlioz, P. Bortolotti, V. Cros, K. Yakushiji, A. Fukushima, H. Kubota, S. Yuasa, M. D. Stiles, and J. Grollier, *Nature* **547**, 428 (2017).
- [45] A. Vansteenkiste, J. Leliaert, M. Dvornik, M. Helsen, F. Garcia-Sánchez, and B. Van Waeyenberge, *AIP Advances* **4**, 107133 (2014).
- 
- Acknowledgments.** We acknowledge Franck Ernult and Albert Fert for insightful discussions, and Wen Siang Lew for allowing us to access his instruments. We acknowledge the support of the A\*STAR Computational Resource Center (A\*CRC), Singapore and the National Supercomputing Centre (NSCC), Singapore for performing computational work. This work was supported by the A\*STAR Pharos Fund (Ref. No. 1527400026) of Singapore, the Singapore Ministry of Education (MoE), Academic Research Fund Tier 2 (Ref. No. MOE2014-T2-1-050), and the National Research Foundation (NRF) of Singapore, NRF – Investigatorship (Ref. No.: NRF-NRFI2015-04).
- Author Contributions.** P.H., A.S., and C.P. designed and initiated the research. M.R. deposited the films and characterized them with A.S. and A.K.C.T. P.H. and L.S.H. fabricated the nanostructures. P.H. and A.K.C.T. performed the MFM and analyzed the imaging data with A.S. G.S. and A.L.G.O. performed the micromagnetic simulations. A.S. and C.P. coordinated the project. All authors discussed the results and provided inputs to the manuscript.
- 
- F. METHODS**
- Film Deposition.** Multilayer stacks consisting of: Ta(30)/Pt(100)/[Ir(10)/Fe( $x$ )/Co( $y$ )/Pt(10)]<sub>20</sub>/Pt(20) (nominal layer thicknesses in Å in parentheses) were deposited on thermally oxidized 100 mm Si wafers by DC magnetron sputtering at RT using a Chiron™ UHV system manufactured by Bestec GmbH. The deposition was performed with base pressure below  $10^{-8}$  Torr, and a working pressure of  $2 \times 10^{-3}$  Torr was maintained during deposition. Five Fe( $x$ )/Co( $y$ ) compositions are investigated here: Fe(2)/Co(6), Fe(2)/Co(5), Fe(3)/Co(6), Fe(4)/Co(6), and Fe(5)/Co(5). Varying the Fe( $x$ )/Co( $y$ ) composition enables modulation of the magnetic parameters –  $K_{\text{eff}}$ ,  $D$ , and  $\kappa$  – for this work (see §SI 1). These parameters have been quantified previously<sup>10</sup>.
- Dot Fabrication.** Negative resist Ma-N 2403 was spin-coated on the multilayer films to form a  $\sim$  300 nm thick overlayer. Dots of diameter ( $W$ ) 100–3000 nm were defined using an Elionix™ electron beam lithography tool. The patterns were transferred onto the multilayer films using an Intlvac™ ion beam etching system, with residual resist lifted off in an ultrasonic bath. Feature topography was imaged using a Veeco Dimension™ 3100 scanning probe microscope, and a JEOL™ JSM- 7401 field emission SEM. Cross-sectional SEM images (e.g. Fig. 1c) were obtained by tilting the sample at nearly

90°, with the sample mounted on a vertical holder. Structural characterization of the dots shows an upright profile with relatively constant diameter vertically through the stacks for  $W = 200 - 500$  nm (see [SSI 2](#)). For dots with  $W \leq 150$  nm, a resist overlayer, due to incomplete lift-off, was observed in numerous cases (e.g. [Fig. 4b-i](#),  $W = 150$  nm). The resulting low yield for  $W \leq 150$  nm precludes a direct comparison of magnetic phases across samples.

The magnetization properties of  $W \geq 500$  nm dots were found to be consistent with film level results (see [SSI 3](#)). While AFM images do show some skirting effects at the bottom boundary, the magnetic layers at the taper are too thin to contribute a detectable signal in MFM images.

**MFM Measurements.** MFM imaging was performed using a Veeco Dimension™ 3100 scanning probe microscope, with Co-alloy coated SSS-MFMR™ tips. The sharp tip profile (diameter~30 nm), its ultra-low moment ( $\sim 80$  emu cm $^{-3}$ ), and lift heights of 20-30 nm used during scanning provided high-resolution MFM images, while introducing minimal stray field perturbations. The dots were imaged after *ex situ* negative OP saturation, followed by the application of *in situ* OP fields ranging from 0 to 200 mT. Repeated MFM scans were acquired to ensure consistency and reproducibility of results. Twelve dots were imaged for each  $W$  and Fe/Co composition to mitigate variability in deposition and fabrication processes.

**Micromagnetic Simulations.** Micromagnetic simulations were performed using mumax<sup>3</sup>-based simulation software<sup>45</sup>. The dot was defined with a cylindrical geometry, in line with experimentally fabricated structures. The mesh cell size used had lateral dimensions of  $2 - 4 \times 2 - 4$  nm $^2$ , while the vertical size  $t_{\text{FM}}$  was set to match the Fe/Co magnetic layer thickness of each sample (e.g.  $t_{\text{FM}} = 0.8$  nm for Fe(2)/Co(6)). A  $\sim 2$  nm spacer layer was introduced between magnetic layers (for Ir and Pt), with

the spacer thickness approximated to be the nearest multiple of  $t_{\text{FM}}$ . The results shown correspond to simulations of 20 stack repeats, consistent with the experimental multilayer film. Single stack simulations were performed for illustrative comparisons. The magnetic parameters  $M_S$ ,  $K_{\text{eff}}$ ,  $A$ ,  $D_c$ , and  $D$  used were consistent with our film level results on [Ir/Co( $x$ )/Fe( $y$ )/Pt]<sub>20</sub> stacks<sup>10</sup> (see [SSI 1](#)), and the Gilbert damping parameter  $\alpha$  was set to 0.1. A single (or multiple) skyrmion configuration was initialized in the dot, and the magnetization was allowed to relax to simulate the ZF configuration for each set of parameters (see [SSI 4](#)). For [Fig. 3b-c](#), bi-linear interpolation was used to map the boundary regions between the different magnetic states.

MFM images were generated from the 2D magnetization profile using the mumax<sup>3</sup> built-in MFM function<sup>45</sup>, with a tip height of 20 nm and dipole size

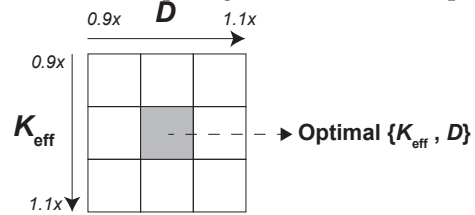


**FIG. M1. Parametric Array for Phase Diagram.** A weighted average of a  $3 \times 3$  array, corresponding 10% variations in  $D$  and  $K_{\text{eff}}$  with respect to optimal values ([SSI 1](#)), is used to determine the expected magnetic state from micromagnetic simulations of the dots in [Fig. 3d](#).

of 30 nm respectively.

A weighted average method was adopted to determine the expected magnetic phase evolution with varying  $W$  ([Fig. 3d](#)). A  $3 \times 3$  array of  $D$  and  $K_{\text{eff}}$  values was used ([Fig. M1](#)), with the upper and lower limits corresponding to  $\pm 10\%$  with respect to the optimal values determined previously. The observation of UM, SK and LS states for each pair of parameters were assigned weights of -1, 0, and +1 respectively. The total weight of the array was used to estimate the expected magnetic state for each  $W$ .